Journal of
Composites Science

MDPI

Article

Micro-Level Hybridization of Steel, Glass, and Polypropylene Filaments via Air Texturing: Mechanical and Morphological Analysis

Jan Rehra [1,*], Matthias Overberg [2], Sebastian Schmeer [3], Anwar Abdkader [2] and Chokri Cherif [2]

[1] Deutsches Zentrum für Luft- und Raumfahrt e.V., Institut für Systemleichtbau, Lilienthalplatz 7, 38108 Braunschweig, Germany
[2] Faculty of Mechanical Science and Engineering, Institute of Textile Machinery and High-Performance Material Technology (ITM), Technical University Dresden, 01069 Dresden, Germany; matthias.overberg@tu-dresden.de (M.O.)
[3] Leibniz Institut für Verbundwerkstoffe, Erwin-Schrödinger-Straße 58, 67655 Kaiserslautern, Germany
* Correspondence: jan.rehra@dlr.de; Tel.: +49-531-295-1526

Abstract: The increasing application of fiber-reinforced polymer (FRP) composites necessitates the development of composite structures that exhibit high stiffness, high strength, and favorable failure behavior to endure complex loading scenarios and improve damage tolerance. Achieving these properties can be facilitated by integrating conventional FRPCs with metallic materials, which offer high ductility and superior energy absorption capabilities. However, there is a lack of effective solutions for the micro-level hybridization of high-performance filament yarns, metal filament yarns, and thermoplastic filament yarns. This study aims to investigate the hybridization of multi-material components at the micro-level using the air-texturing process. The focus is on investigating the morphological and the mechanical properties as well as the damage behavior in relation to the process parameters of the air-texturing process. The process-induced property changes were evaluated throughout the entire process, starting from the individual components, through the hybridization process, and up to the tape production. Tensile tests on multifilament yarns and tape revealed that the strength of the hybrid materials is significantly reduced due to the hybridization process inducing fiber damage. Morphological analyses using 3D scans and micrographs demonstrated that the degree of hybridization is enhanced due to the application of air pressure during the hybridization process. However, this phenomenon is also influenced by the flow movement of the PP matrix during the consolidation stage. The hybrid laminates exhibited a damage behavior that differs from the established behavior of layer-separated metal fiber hybrids, thereby supporting other failure and energy absorption mechanisms, such as fiber pull-out.

Keywords: metal fiber hybrids; homogeneous fiber hybridization; morphology characterization; mechanical characterization; damage behavior

Academic Editor: Chensong Dong

Received: 8 November 2024
Revised: 16 December 2024
Accepted: 17 December 2024
Published: 2 January 2025

Citation: Rehra, J.; Overberg, M.; Schmeer, S.; Abdkader, A.; Cherif, C. Micro-Level Hybridization of Steel, Glass, and Polypropylene Filaments via Air Texturing: Mechanical and Morphological Analysis. *J. Compos. Sci.* **2025**, *9*, 12. https://doi.org/10.3390/jcs9010012

1. Introduction

1.1. State of the Art

Various methods have been investigated to improve the damage tolerance and energy absorption of fiber-reinforced plastics, including the improvement of matrix toughness [1], the hybridization of fibers [2], and the development of 3D composites [3]. In this study, a hybridization approach is pursued to improve the failure behavior by incorporating ductile metal material into the laminate. A well-known hybridization approach from this

category is macroscopic hybridization on the laminate level, which systematically combines alternating layers of metal sheets and fiber-reinforced plastics (FRPs). These laminates are called fiber–metal laminates (FMLs) [4–6]. However, the layer-by-layer arrangement of FMLs can cause stress concentrations at the interfaces between aluminum foil and fiber-reinforced composite layers, leading to delamination and premature failure [7,8]. This is due to poor interlayer adhesion and low shear stress transferability at the small, constrained interfaces. Improving these interfaces typically requires costly surface treatments like sandblasting, etching, coating, or plasma-based methods [9–11]. High shear stresses during deformation further limit FMLs' applicability for complex geometries. Additionally, FMLs pose economic challenges due to labor-intensive lay-up steps, expensive robotic techniques, costly autoclave processing, long processing times, and significant joining efforts [12]. A further development of this concept, where metal sheets are replaced by metal fibers, so-called metal–fiber hybrids (MFHs), can offer additional advantages. The use of metal fibers instead of sheets allows the application of manufacturing techniques commonly used in fiber-reinforced composites, such as compression molding and vacuum infusion, facilitating the production of more complex structures [13,14]. In addition, due to the significantly larger contact area, the interface between the different reinforcing fibers and the matrix is not problematic [15,16]. There are various investigations on combinations of ductile metallic fibers and conventional high-performance fibers in thermoset or thermoplastic matrices [6,12,17–27]. The improvements in the mechanical material behavior of this MFH can be attributed to the failure mechanism of the hybrid laminate. The ductile material behavior of the metallic fibers allows for further load carrying after the brittle failure of the classical reinforcement component—the so-called initial failure. The performance of the metal fiber hybrid composite, especially in post-failure behavior, depends primarily on the properties of the constituents and their composition. Although most studies on MFHs focus on a layer-separated hybridization concept, in principle, there are three general levels of hybridization (see Figure 1) [14].

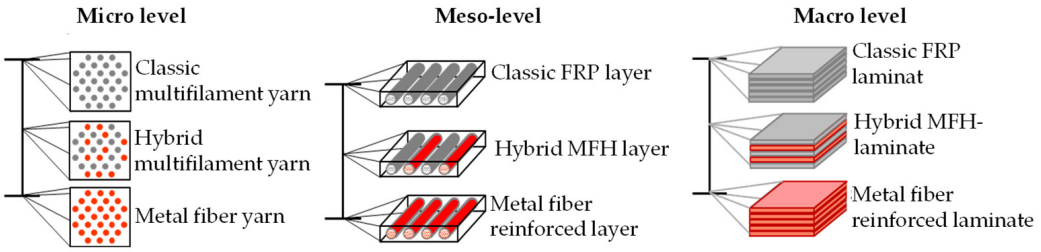

Figure 1. Three general levels of hybridization for laminated composites, according to [14].

The drawbacks of MFHs arise from the stiffness differences between metal fibers and the matrix, leading to micromechanical stresses in transversely loaded structures. Especially for layer-separated hybridization concepts, which result in locally dense packing of metal fibers with resin-rich areas surrounding them, the effects of micromechanical stresses lead to influences on the corresponding shear and transversal tensile behavior of FMHs. Moreover, under realistic stress conditions with local stress peaks, plastic necking of the steel fibers occurs only in locally limited areas, causing local fiber detachment. Due to the layer-separated MFH concept, these local fiber detachments rapidly grow into delamination between the metallic reinforced layers and the conventional reinforced layers [19]. In accordance with the size of the local delamination, enhancements in energy absorption can only be achieved with higher metal fiber contents. MFHs with a small metal fiber volume often exhibit brittle failure in the material behavior [19].

1.2. Challenge

By developing an MFH with hybridization based on micro-level mixing, the disadvantages of the layer-separated MFH concept can be improved. Compared to the layer-separated MFH concepts, the homogeneous dispersion of steel fibers and high-performance filaments can reduce morphologically induced local stress concentrations. In addition, local fiber detachment due to plastic necking is not expected to lead directly to delamination for a hybrid on the micro-level [17]. Furthermore, the close proximity of different fiber types in highly dispersed MFHs enables a more homogeneous load transfer and activates additional failure and energy absorption mechanisms, such as fiber pull-out [17]. For the manufacturing of highly dispersed MFHs, typically, hybrid yarns are needed. There are numerous basic technologies for producing hybrid yarns, including friction-spun staple fiber hybrid yarns, ply yarns, carded yarns, twisted yarns, and commingling yarns [13]. A promising approach is the hybridization of yarns using air jet technologies [28]. The air jet texturing process involves the mixing and twisting of filaments by feeding them through an air jet, creating alternating compact and open yarn structures. The properties of the resulting yarns depend on several factors, including the process parameters, nozzle geometry, and the characteristics of the filaments used [29]. However, research has mostly focused on the combination of two classic FRP materials, while the manufacturing of hybrid yarns from metal, high-performance, and thermoplastic filaments has hardly been investigated [30–32]. Therefore, the development of multi-material hybrid yarns with homogeneous mixing of metal and high-performance fibers is a challenging task. This particularly applies when regarding the processing of fiber components with different properties, such as bending stiffness and density. In addition, hybridization with air jet technology is accompanied by process-related fiber damage and undulation, which counteract the advantages of the homogeneous mixed hybridization partners for the material concept of MFHs.

1.3. Objective

The objective of this study is to examine the morphological and mechanical characteristics of a multi-material hybrid yarn as well as its laminates, comprising glass, steel, and polypropylene (PP) filament yarns with micro-level hybridization. Hybrid yarns are manufactured using an air jet technology-based process. The laminates are manufactured via thermoforming in a heat press. In a previous paper [33], the adaption of air jet texturing technology as well as the development of multi-material hybrid yarns from glass, steel, and polypropylene was reported. This study focuses on investigating the process-related changes in properties throughout the manufacturing process, from the initial properties of the individual filaments to the hybridization process and finally to laminate manufacturing. The tensile properties, morphological properties, degree of damage, and degree of undulation of the different yarn and tape structures are analyzed and evaluated based on selected process parameters of the air jet texturing process.

2. Experimental Setup and Methodology

2.1. Materials

The production of the multi-material hybrid yarns involved the use of stainless-steel (SF), glass (GF), and polypropylene (PP) filament yarns. The properties of these filament yarns are presented in Table 1. The GF and PP yarns were employed in their original state, while the SF yarn was created through the combination of ten stainless-steel monofilaments.

Table 1. Filaments yarns used for manufacturing hybrid yarns.

	Glas Fiber (GF)	Steel Fiber (SF)	PP Fiber (PP)
Supplier	P-D Glasseiden GmbH Oschatz, Wellerswalder Weg 17, D-04758 Oschatz, Germany	Heinrich Stamm GmbH, Grüner Talstraße 125 58644 Iserlohn · Germany	Chemosvit Fibrochem, s.r.o, Štúrova 2/101, 059 21 Svit, Slovakia
Product label	EC9	1.4301	Prolen H EC 330/200
Density [g/cm^3]	1.77	7.95 ± 0.01	0.89
Diameter [µm]	8.5 ± 1.09	59.4 ± 1.29	15
Melt-Flow-Rate-Index [g/10 min]	-	-	25

2.2. Hybridization

The hybridization was carried out using an air jet texturing machine (type RMT-D, Stähle) to produce multi-material hybrid yarns from stainless-steel (SF), glass (GF), and polypropylene (PP) filament yarns (see Figure 2).

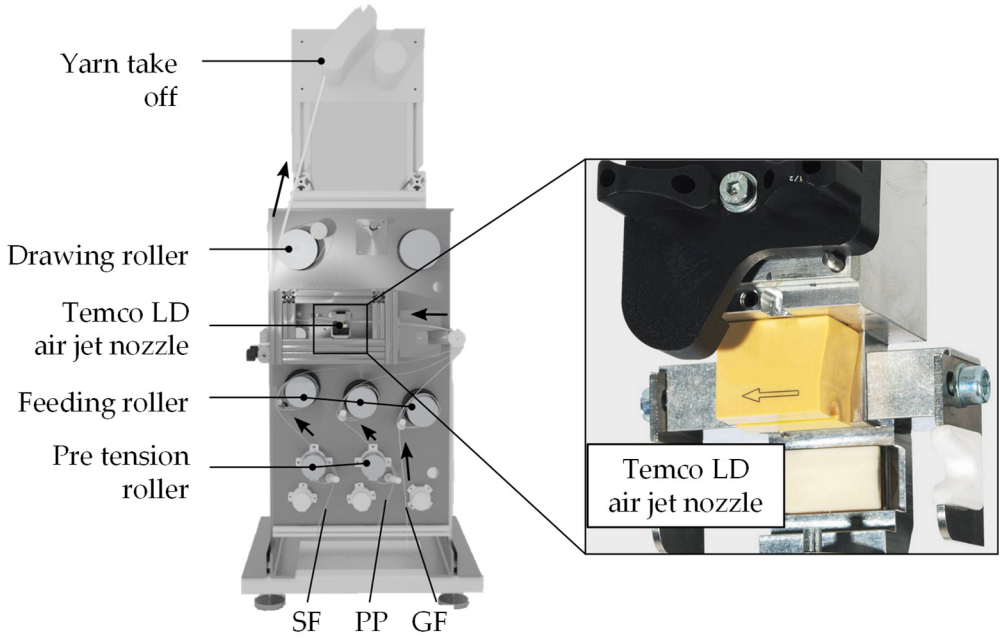

Figure 2. Manufacturing hybrid multi-material yarns using air jet texturing machine along the direction of the arrow.

These single-component yarns were fed separately via godet pairs and aerodynamically blended using a mixing air jet nozzle (Temco LD 32.04). This setup facilitated filament opening by overfeeding the filaments (7% overfeed). Various hybrid yarns were produced by varying the air pressure from 2.0 to 5.0 bar at a constant feed speed of 30 m/min. The yarns we produced had a theoretical fineness of 490 tex with a weight ratio of 43/43/14 for the SF, GF and PP, components. Hot air (180 °C) was used to reduce the viscosity of the sizing on the GF filaments to facilitate their separation. As a reference, hybrid yarns have been produced that represent a "SidebySide" approach (SBS). They have been made by simply fusing the single-component yarns together to form a hybrid multifilament yarn. As these hybrid yarns are not treated by the air jet texturing machine, they are not accompanied by hybridization process-related fiber damage and undulation. Therefore, the SBS configurations are suitable as a comparison partner. All yarns aim for a steel fiber volume fraction of 18.2 vol.%, a glass fiber volume fraction of 40.4 vol.%, and a PP volume fraction of 41.4 vol.%. Table 2 summarizes the hybrid yarns produced under various processing conditions using the conventional air-jet texturing machine.

Table 2. Overview of the manufactured hybrid multifilament yarns.

Label	Fineness of Filament Yarns (tex)			Overfeed	Air Pressure	Linear Density of Hybrid Yarn (tex)
	SF	GF	PP	(%)	(bar)	
SBS	1 × 225	3 × 68	2 × 33	-	-	422
2 bar				7	2	
3 bar				7	3	
4 bar				7	4	
5 bar				7	5	

2.3. Tape Manufacturing

MFH tapes were produced using a specially designed winding unit in combination with a press tool adapted to the tape geometry (see Figure 3a). The hybrid multifilament yarn was fed to the winding unit through a yarn guide, which allowed for the systematic positioning of the hybrid yarns. The winding unit consisted of a frame and two winding shafts. The winding shafts were provided with slots and allowed the hybrid yarns to be deposited in a targeted manner. A pre-tension device ensured that the winding shaft could move inwards during the pressing process to prevent the fibers from tearing and to apply a targeted pre-tensioning force. Silicone pads were used to balance the different tensions of the individual hybrid yarns.

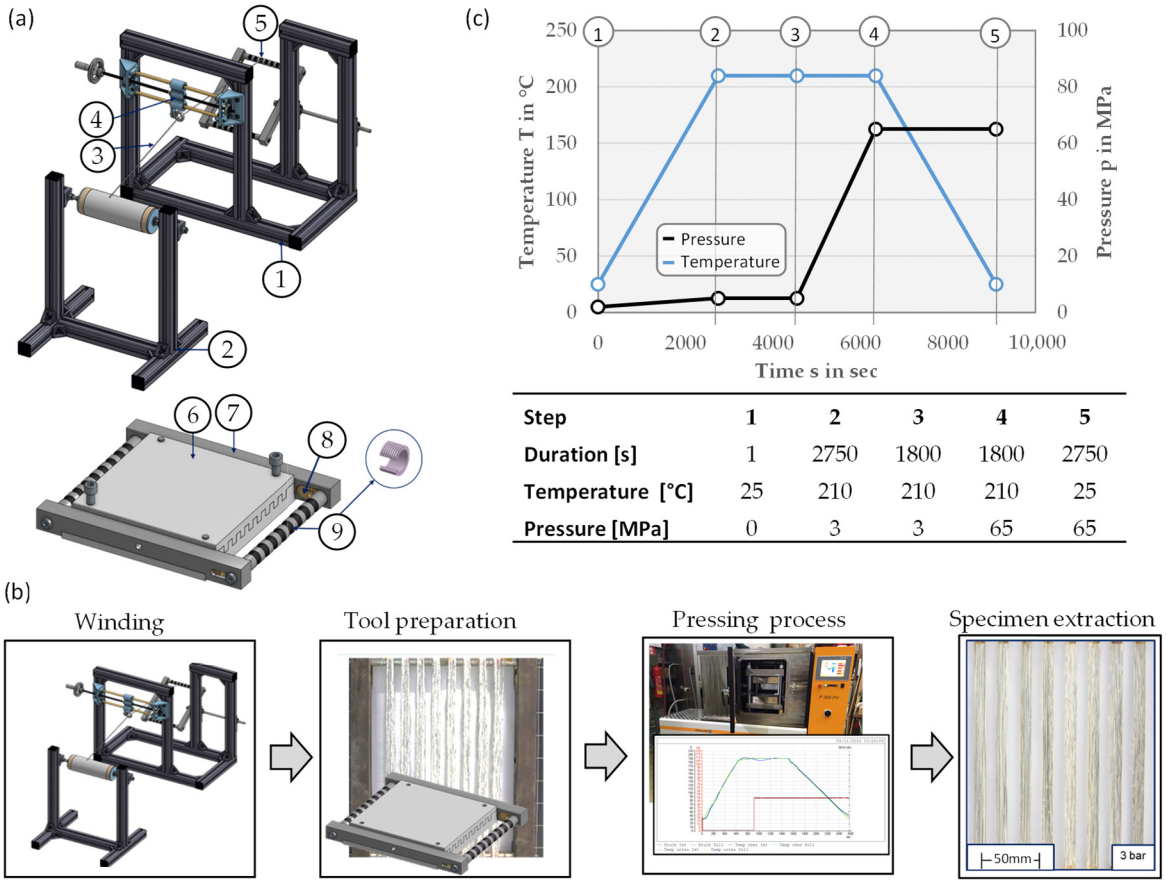

Step	1	2	3	4	5
Duration [s]	1	2750	1800	1800	2750
Temperature [°C]	25	210	210	210	25
Pressure [MPa]	0	3	3	65	65

1 Winding setup. **2** Bobbin holder. **3** Hybrid multi-filament yarn. **4** Yarn guide. **5** Winding unit. **6** Pressing tool. **7** Winding frame. **8** Pre-tension device. **9** Silicone pads.

Figure 3. (**a**) Winding unit and press tool adapted to the tape geometry, (**b**) process overview of the tape manufacturing, and (**c**) time–temperature profile of the press process.

The manufacturing process is shown in Figure 3b. Eight windings were used for each tape. The distance between the windings was 1.12 mm. After winding, a pressing process

was carried out to produce the samples. This was achieved using a specially designed pressing tool consisting of a base plate and a press stamp. Analog to the winding unit, the base plate and press stamp have slots into which the hybrid yarns are pressed when the pressing tool is closed. The UD tapes were consolidated using the P300 PV thermal laboratory press from COLLIN Lab & Pilot Solutions GmbH (Gewerbestraße 11, 83558 Maitenbeth, Germany) at a temperature of 210 °C and a pressure of 65 MPa. The used time–temperature profile is shown in Figure 3c.

2.4. Mechanical Characterization

Mechanical characterization was carried out in parallel to the production process of the hybrid tapes and refers to the single filaments before hybridization, to the hybrid yarns after hybridization, and to the hybrid tapes after laminate production. The mechanical characterization of the single filaments was carried out by single-filament tensile tests. The stress–strain behavior of single GF filaments were tested using the Vibromat ME from Textechno, Mönchengladbach, Germany. The tests were performed according to DIN EN ISO 5079 [34]. A test length of 20 mm, a crosshead speed of 0.15 mm/s, and a load cell of 100 N were used. The tensile tests on the stainless-steel filaments were conducted using a modified hydraulic tensile testing machine (Zwick Roell HTM 5020) (see Figure 4a). For these tests, specimens with a total length of 160 mm and a gauge length of 100 mm were tested with a crosshead speed 1 mm/s. To simplify specimen handling and to avoid clamp breakage or slipping, the specimens were provided with 30 mm end taps made of adhesive tape. Deformation was measured using a high-speed camera system combined with optical motion tracking of the clamping devices. Force measurement was performed with a piezoelectric load cell calibrated to 50 N. The test result for the SF, GF and PP filaments were analyzed on basis of 50 single filament tests. The mechanical properties of the multifilament yarns were evaluated using an identical test setup and specimen size as the ones employed for the single-filament tests. The calibrated range of the piezoelectric load cell was modified to 1 kN for force measurement for these tests. For each hybrid yarn configuration, 30 specimens were tested.

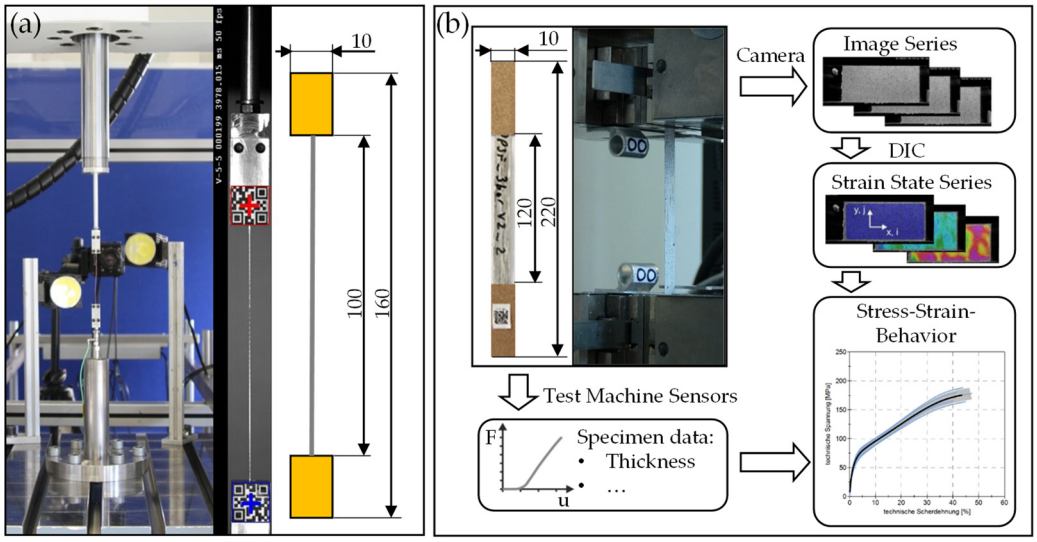

Figure 4. (**a**) Test setup for single and multifilament testing; (**b**) setup for laminate testing.

For the mechanical characterization of the MFH tapes, we performed a tensile test according to DIN EN ISO 527 [35] using a servo-electric testing machine of the type Zwick/Roell Z250 (Shanghai, China) (see Figure 4b). The specimens were fitted with end tabs to enhance load application by the hydraulic grips of the test machine. A load cell with

a calibrated range up to 10 kN was used to measure the force, while a three-dimensional digital image correlator (DIC) was applied to record the specimen strain. Data acquisition started when the force exceeded a threshold of 10 N and stopped when it fell below this threshold. Eight specimens were tested for each MFH tape configuration. All tests were conducted under laboratory conditions at a room temperature of 23 °C. The forces and deformations were analyzed using engineering stresses and strains. Additionally, the stress–strain behavior of all hybrid yarns and tapes was analyzed with regard to their characteristic properties (see Figure 5).

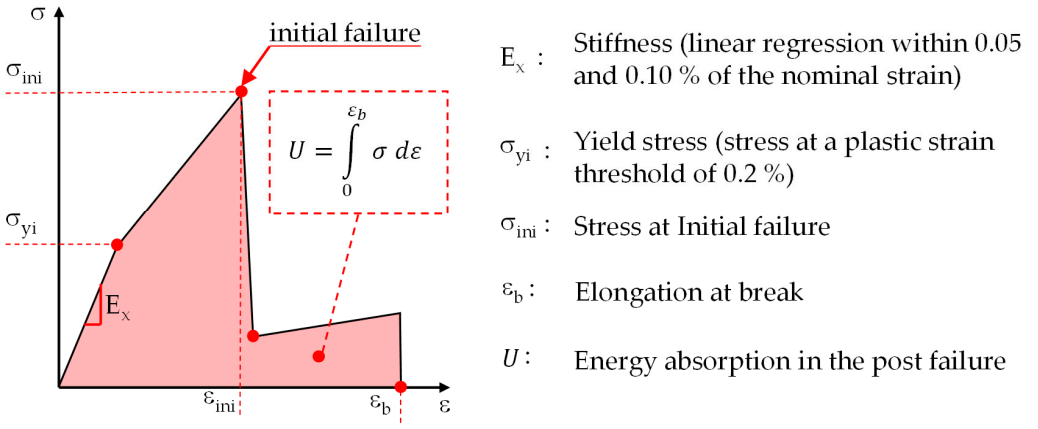

Figure 5. Qualitative stress–strain behavior of SCFRP, including its characteristic properties.

2.5. Analyses of the Material Microstructure

To analyze the damage caused by the initial failure, additional tensile tests were carried out and stopped immediately after the initial failure. The specimens were then removed from the testing machine and further processed for microstructural analysis. For this purpose, 2D radiographic images were taken under an X-ray microscope, namely, the Zeiss Xradia 520 Versa (Zeiss, Oberkochen, Germany). The parameter set used for taking radiographic images is listed below (see Table 3). In order to obtain a complete image of the specimen, two scans were required: one of the upper portion and one of the lower portion. A marked label on the specimen has been used to facilitate the merging of the two images. The label was applied with a colored ink containing metal particles, which allowed for the visibility of the mark in the X-ray microscope. Further microstructural investigations were conducted on the hybrid multifilament yarns and hybrid tapes. For this purpose, three-dimensional microstructure determinations were performed using the same X-ray microscope. To mount the hybrid yarn sections in the X-ray microscope, the yarns were stitched into opaque foam material and mounted to a sample holder. The MFH tapes were analyzed on small tape sections, which could be mounted directly. The parameter settings utilized for these investigations are presented in Table 3.

Table 3. Parameter sets used for radiographic images.

Parameter	Units	2D Radiographic Images	3D Analysis of Yarn	3D Analysis of Tape
Voltage	keV	70	90	90
Current	µA	85.7	95.2	95.2
Pixel/voxel size	µm	28.54	1.021	0.721
Magnification factor		0.4	0.4	0.4
Exposure time	s	6	6	6
ROI	Pixel	500 × 2000	2000 × 2000	2000 × 2000

The resulting grayscale image series were further processed to separate different material phases and derive the geometric information (see Figure 6). Therefore, different

filter and segmentation algorithms implemented in GeoDict 2023 were used. First, a non-local means filter with a patch size of 2 voxels and a search radius of 3 voxels was used for noise reduction. Afterwards, a segmentation algorithm based on the random forest model with 100 trees and a depth of 6 levels was trained on selected grayscale images and applied to the whole series for segmentation. To derive geometric information, fiber identification was performed for each segmented image using a Hough circle detection algorithm implemented in a Python subroutine based on the OpenCV library. To derive the 3-dimensional centerline geometry of the fibers, the circles that had been found in every image were connected to a circle with similar centerpoint coordinates in the following images. Finally, a fiber type assignment based on the circle diameter was carried out.

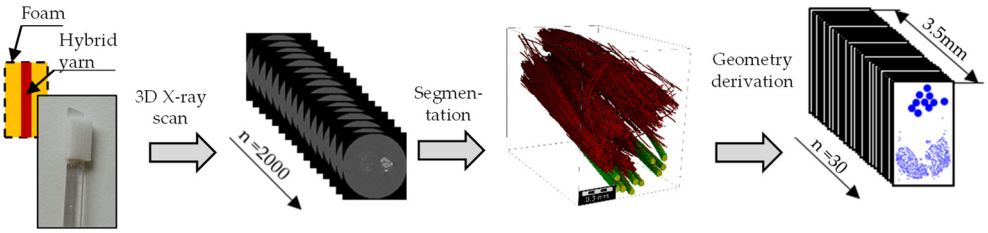

Figure 6. Overview of the process for determining the geometry information of hybrid yarn and tape morphologies.

These sets of geometrical information were further processed to determine the degree of undulation, fiber orientation deviation, as well as the degree of dispersion. The fiber orientation deviation was quantified by measuring the angle between the reference edge of the region of interest (ROI) and a line defined by the start and end points of each fiber. The degree of undulation Θ was calculated based on the ratio of the length of the 3-dimensional centerline $\hat{l}$ of a fiber and the distance between its start and its end point l (see Formula (1)).

$$\Theta = \frac{\hat{l}}{l} \tag{1}$$

Although there is a well-established methodology for quantifying undulation, there is currently no accepted standard for measuring dispersion. This lack of a standardized definition for dispersion hinders the ability to assess the scattering of multiple object types within a given area. There are several methods for evaluating the distribution of fibers within a fiber matrix architecture through statistical point pattern analysis. Accordingly, a parameter for the quantitative assessment of the degree of dispersion was developed. Therefore, the centerpoint coordinates in each image were treated as individual point patterns for the steel fibers P_{sf} and the glass fibers P_{gf}, where

$$P_{gf/sf} = \left\{ \left(x_{i\ sf/gf}, y_{i\ sf/gf} \right) \right\} \quad for \quad i \in \{1, 2, \ldots n\} \tag{2}$$

In order to facilitate the subsequent analysis of the dispersion, the region of interest (ROI) in each image was divided into a set of subsections M, where

$$M = (M_1, M_2, ..., M_m)\ for\ j \in \{1, 2, \ldots m\} \tag{3}$$

Each subsection was defined by its lower and upper boundary in each direction (see Formula (4)).

$$M_j \left(x_{j\ min}, x_{j\ max}, y_{j\ min}, y_{j\ max} \right) \tag{4}$$

Subsequently, the points of each point pattern that fell within the boundary of a subsection were counted and assigned a respective subsection count N_j (see Formula (5)).

$$N_{j\ sf/gf} = \sum_{i=1}^{n} 1\left(x_{j\ min} \leq x_{i\ sf/gf} < x_{j\ max} \bigwedge y_{j\ min} \leq y_{i\ sf/gf} < y_{j\ max}\right) \quad (5)$$

An example of the resulting local density evaluation for the point pattern of a hybrid yarn configuration is illustrated in Figure 7a.

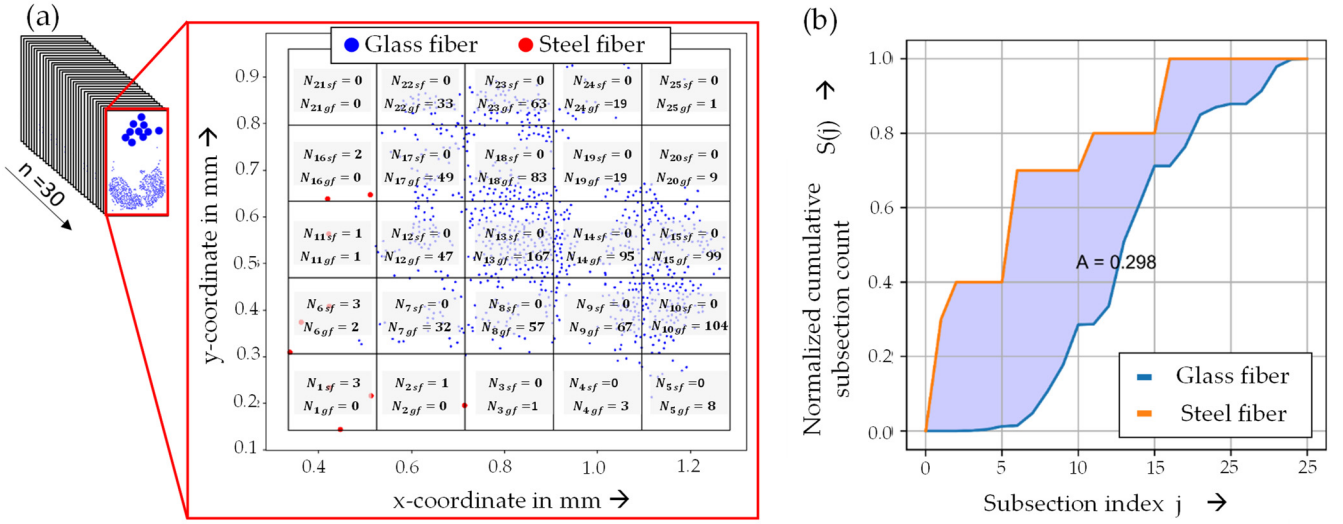

Figure 7. (**a**) Local density evaluation for the point pattern of a hybrid yarn and (**b**) iterative accumulation of the normalized subsection counts for steel fibers and glass fibers over the total number of subsections.

This local density evaluation was further used to determine the iterative accumulation of the normalized subsection counts for steel fibers and glass fibers over the total number of subsections (see Equations (6)–(8)/Figure 7b).

$$S_0 = 0 \quad (6)$$

$$S_{j\ sf/gf} = S_{j-1\ sf/gf} + \frac{N_{j\ sf/gf}}{\sum_{j=0}^{m} N_{j\ sf/gf}} \quad fr \quad j \in \{1, 2, \ldots m\} \quad (7)$$

$$S_{sf/gf} = \left(S_{0\ sf/gf}, S_{1\ sf/gf}, \ldots, S_{m\ sf/gf}\right) \quad (8)$$

The resulting lists of normalized and incrementally accumulated subsection counts S can then be used to define a criterium for the dispersion of different fiber types within a point pattern. In an ideal homogeneous dispersed hybrid yarn or tape, the curves of the incrementally accumulated subsection counts of steel fibers and glass fibers are superimposed. This can be expressed as the ratio between the steel fibers in a subsection and the total number of steel fibers in the ROI being identical to the ratio between the glass fibers in the subsection and the total number of glass fibers in the ROI for each subsection. In the event that the dispersion deviates from ideal homogeneity, the two curves enclose an area whose size enables the quantitative evaluation of dispersion. Therefore, the enclosed area A between the curves of the incrementally accumulated subsection counts can be determined using the following integral:

$$A = \frac{1}{m} \int_{j=1}^{m} \left| S_{j\ sf} - S_{j\ gf} \right| dj \quad (9)$$

Given that the degree of hybridization is related to the size of the subsection, it is necessary to provide the edge length of the subsection as well. The degree of hybridization

converges to $A = 1$ for strongly separated steel fibers and glass fibers and converges to $A = 0$ for an ideal homogeneous dispersion (see Figure 8).

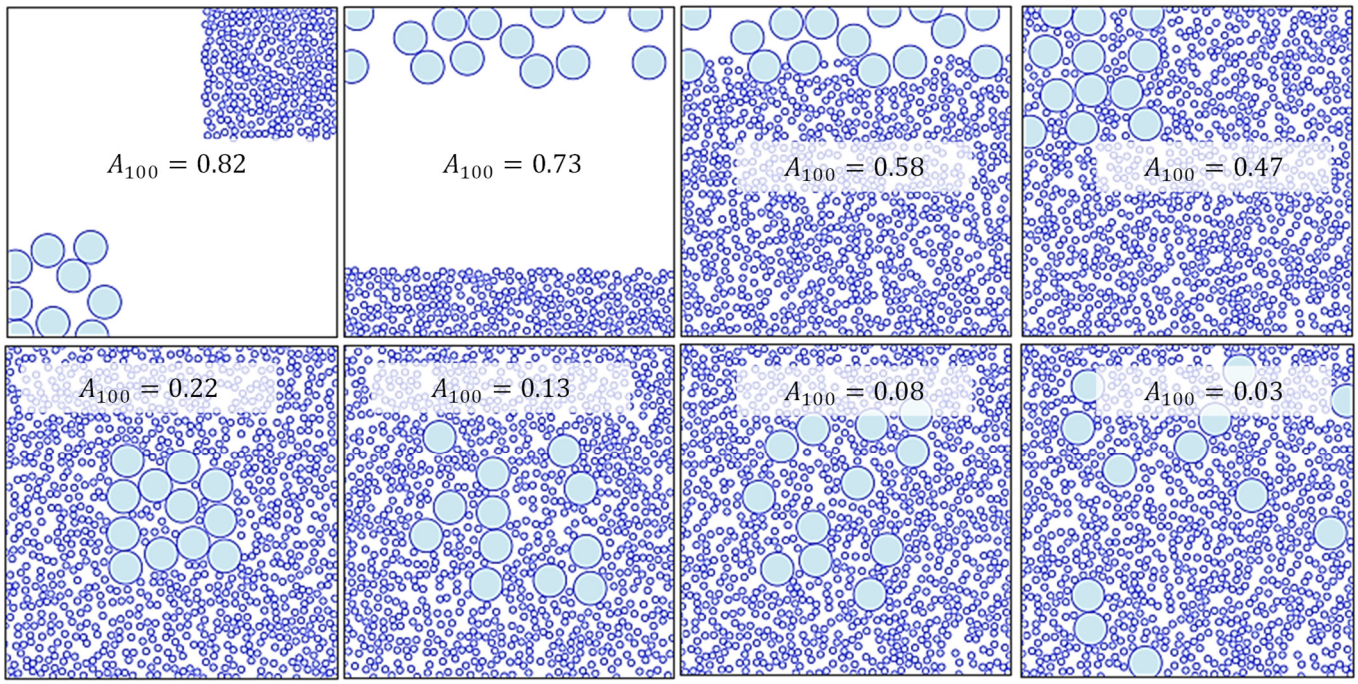

Figure 8. Exemplary fiber topologies in an ROI of 500 × 500 µm, a subsection size of 100 × 100 µm, and two fiber types ($\varnothing_1$ = 10 µm and $\varnothing_2$ = 50 µm), including the evaluation of the associated degree of hybridization.

In addition to the analysis of the three-dimensional morphology, micrographs of the cross-section of the hybrid tape were employed to analyze fiber volume fractions. For this purpose, samples were extracted from the hybrid yarns and the tapes, embedded, ground, and polished, and micrographs were taken. These micrographs were segmented using threshold values in the gray value spectrum, filtered, and analyzed using a circle detection algorithm based on Hough circle detection.

3. Results and Discussion

3.1. Single Filaments

Figure 9 illustrates the stress–strain curves of the individual glass fiber (GF) and the stainless-steel fiber (SF). The curves of the PP filaments are not included in this figure.

These stress–strain curves are used as references in this work and serve to evaluate the influence of the manufacturing process steps. Since this work considers hybrid yarns and tapes consisting of these components, for the purpose of better comparability, the characteristic values of the single components are superposed according to the composition of the hybrid materials (see Figure 10).

3.2. Hybrid Yarns

The micrographs of the hybrid yarns and the 3D geometries investigated in this study are outlined in Figure 11.

It is evident that the structure of the hybrid yarns undergoes significant widening in response to airflow or rather the air pressure. In contrast, the side-by-side configuration exhibits a compact yarn structure. The steel filaments, in particular, exhibit a pronounced alignment parallel to the yarn axis, irrespective of the air pressure. A widening of the steel fiber bundles can only be observed at higher air pressures of 4 to 5 bar. Due to their high

stiffness and significantly larger diameter, the steel fibers offer much greater resistance to airflow-induced deformation and are therefore only deformed or swirled at high air pressures. In contrast, the glass filaments are much more flexible due to their lower stiffness and smaller diameter and can be deformed and swirled by the airflow even at lower air pressures. This is indicated by the increasing deviation in the fiber orientation and the increased degree of undulation with increasing air pressure (Figure 12a,b). As both types of fibers must be deformed and swirled to achieve homogeneous dispersion using the air jet texturing process, significant changes in the degree of hybridization are only achieved at higher air pressures (Figure 12c).

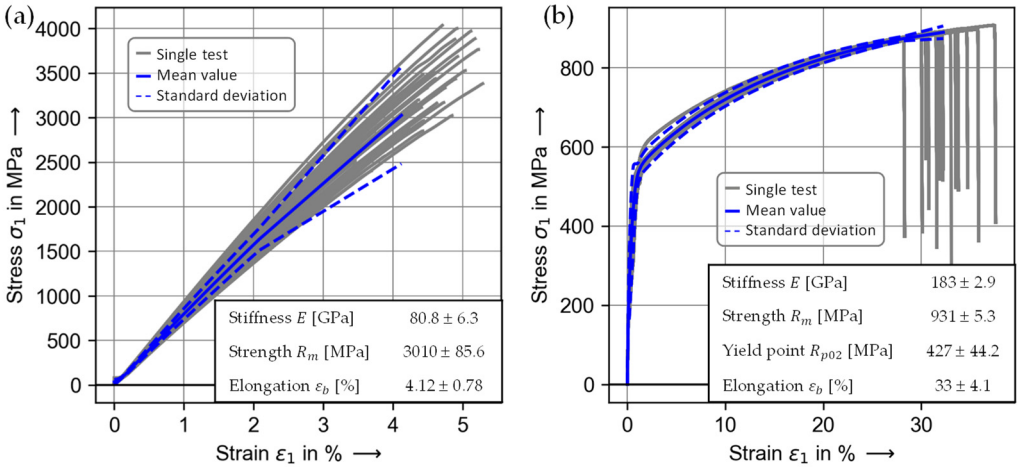

Figure 9. (**a**) Stress–strain curves of the individual glass fiber (GF) and (**b**) the stainless-steel fiber (SF), including the characteristic properties.

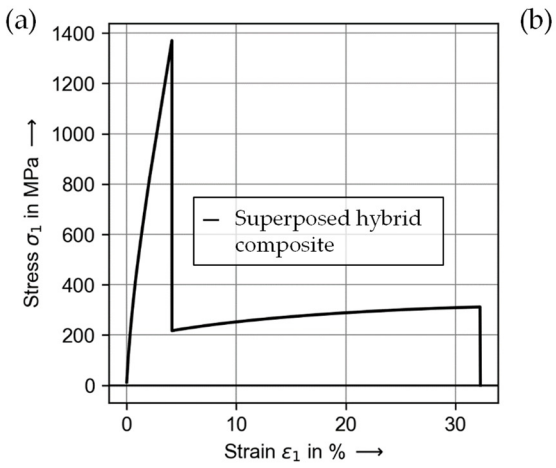

(b)

$$P_{hybrid} = \sum_{components} P_c \cdot \varphi_c$$

P_{hybrid}: Property of the hybrid
P_c: Property of the component
φ_c: Volume fraction of the component

Property of the hybrid	Value
E [GPa]	65.27
σ_{ini} [MPa]	1324.42
σ_{yi} [MPa]	221.42
ε_b [%]	33.41
U [MPa]	95.97

Figure 10. (**a**) Superposed mechanical properties of a hybrid composite with a steel fiber volume fraction of 18.2 vol.%, a glass fiber volume fraction of 40.4 vol.%, and a PP volume fraction of 41.4 vol.%. and (**b**) superposed characteristic properties of the hybrid composite with the corresponding determination equations.

The stress–strain behavior of the hybrid yarns investigated in this study is outlined in Figure 13a using the mean value curves of the corresponding test series. The following Figure 13b–f illustrate the characteristic properties of the stress–strain behavior.

It can be seen in Figure 13b–d that there is a notable decrease in the stiffness, yield stress, and tensile strength of the hybrid yarns with increasing air pressure. The observed behavior correlates with the behavior of the degree of undulation and the deviation in fiber orientation at increased air pressures. Therefore, it is assumed that the degree of undulation and the

deviation in fiber orientation have a particular effect on the stiffness. With regard to the influence of air pressure on strength, it is postulated that the increased flow velocities caused by the high air pressure lead to greater stress on the filaments, which ultimately results in greater damage to the individual filaments. This phenomenon is particularly evident in glass fibers, which are significantly smaller and more sensitive. The mean tensile strength of the side-by-side-configuration is approximately 991 MPa, whereas the configurations produced at 5 bar have an average tensile strength of approximately 606 MPa, which corresponds to a reduction of 32%. In contrast, the measured elongation at break (Figure 13e) and energy absorption (Figure 13f) demonstrate no notable impact from the air pressure. A comparison of the results of the hybrid yarns with the material behavior superposed on the basis of the individual components reveals that the theoretically determined strength (1324 MPa) is notably higher than the strengths of the hybrid yarns (Figure 13a). In contrast, the theoretically determined post-failure behavior matches the behavior of the hybrid yarns to an acceptable degree of accuracy. The post-failure behavior is mainly determined by the steel fibers. The behavior preceding the initial failure is primarily influenced by the interaction of glass and steel fibers, with the glass fibers demonstrating a more pronounced effect. Therefore, it is assumed that the difference between the measured tensile strength of the yarns and the theoretically determined strength of the superposed composite is mainly due to the size effect of the glass fiber properties. The theoretical material behavior is based on the superposition of individual component properties determined in single-fiber tensile tests. It is established that for glass fibers, the probability of a critical failure within the limited length of a single fiber is lower in single-fiber tests, which leads to higher observed strengths. Conversely, in tensile tests on multifilament yarns, the probability of a critical failure increases, as the effective volume and loaded cross-section area are significantly larger. This results in a reduction in the average strength, as the weakest fiber determines the failure of the entire multifilament yarn.

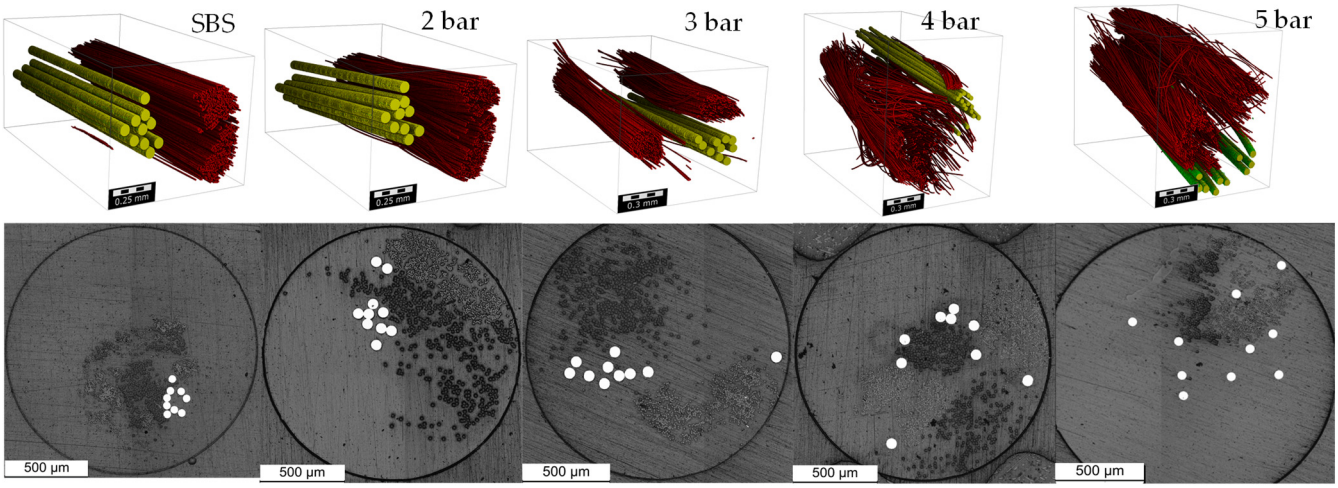

Figure 11. Micrographs and the 3D geometries of the hybrid yarns investigated in this study.

3.3. Hybrid Tapes

The results of the morphology analyses on the hybrid tapes are presented in Figure 14 using 3D scans and micrographs. The determined fiber volume fractions show excellent agreement with the targets set during the hybridization process.

The analysis of the micrographs and 3D scans of the hybrid tapes indicates that the degree of hybridization of exhibits only slight variation (see Figure 15c). However, the originally used yarns demonstrate a notable dependence between the air pressure and the degree of hybridization. It is assumed that this phenomenon is caused by the flow movement of the PP matrix during the production of the tapes in the thermal press. It is

hypothesized that locally melted PP filaments flow into resin-free areas under the pressure within the thermal press, and, due to their comparatively high viscosity, pull or displace both glass fibers and steel fibers with them. This effect is particularly evident in yarns with a low degree of hybridization and poorly mixed PP filaments. Hire, the flow movement results in further intermixing of the steel and glass fibers. In the case of multifilament yarns produced at higher air pressures and with a higher degree of hybridization, the effect of the flow movement is only slightly pronounced. Consequently, the degree of hybridization of the hybrid tapes is identical to that of the hybrid yarns.

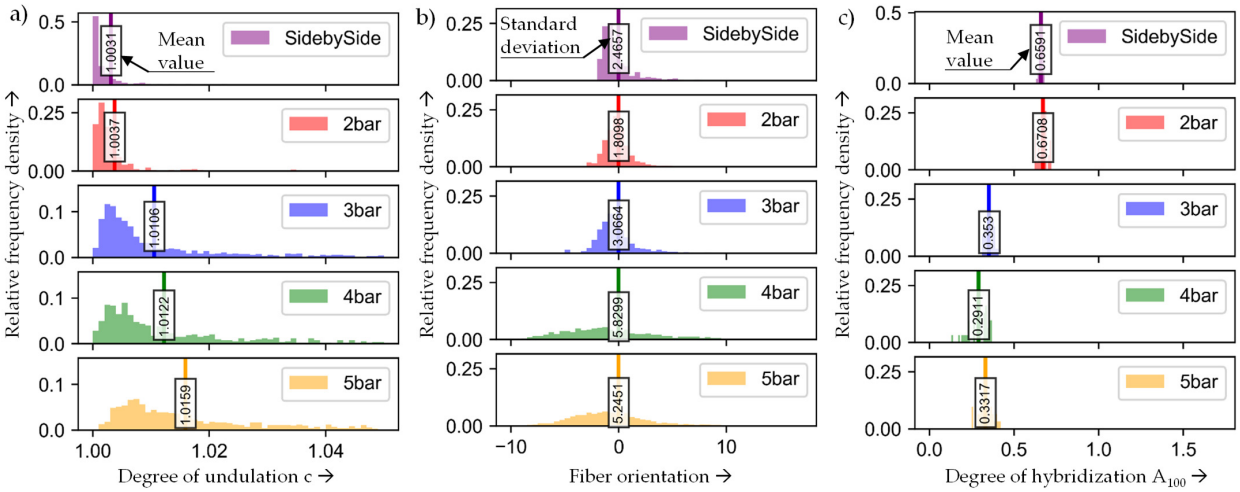

Figure 12. (**a**) The degree of undulation, (**b**) fiber orientation, and (**c**) degree of hybridization of the hybrid yarns investigated in this study.

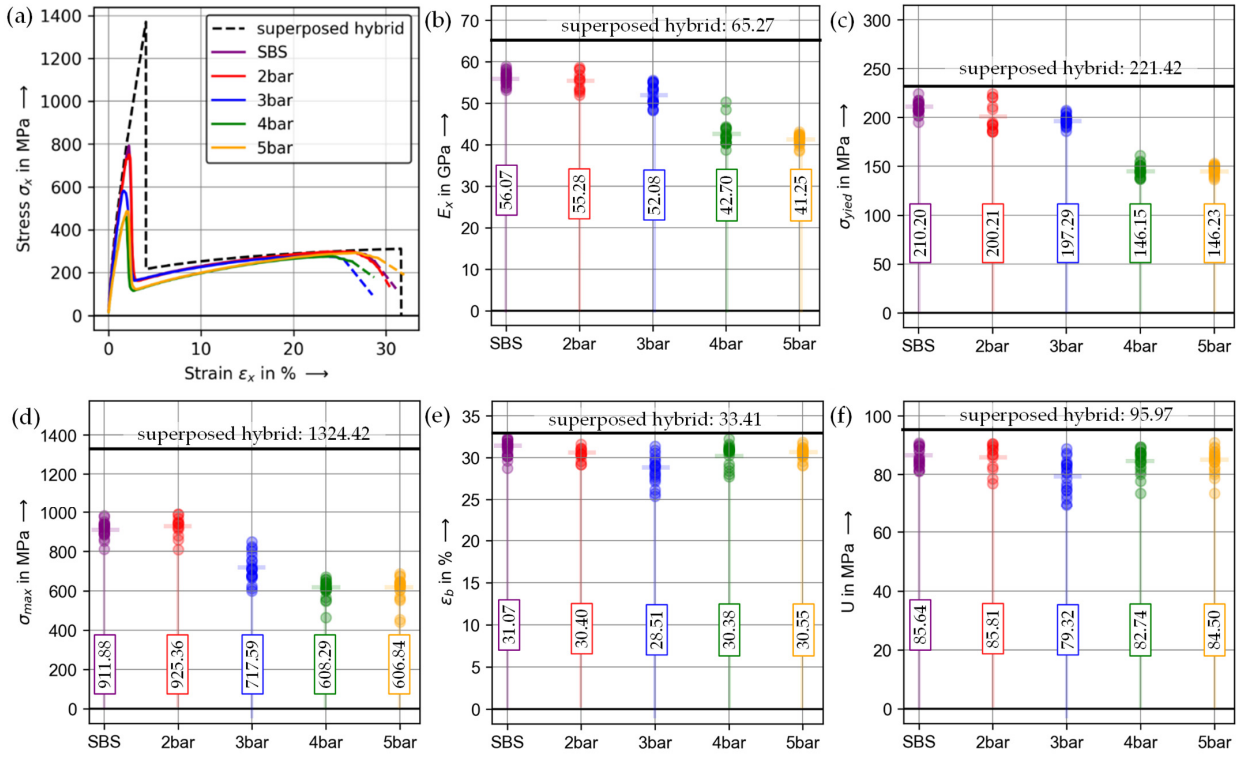

Figure 13. (**a**) Mean curves of the stress–strain behavior of the hybrid yarns, and (**b**–**f**) an overview of the characteristic properties in the stress–strain behavior of the hybrid yarns. This includes the tensile stiffness Ex in (**b**), yield stress σ_{yi} in (**c**), initial failure stress σ_{ini} in (**d**), elongation at break ε_b in (**e**), and energy absorption U in (**f**).

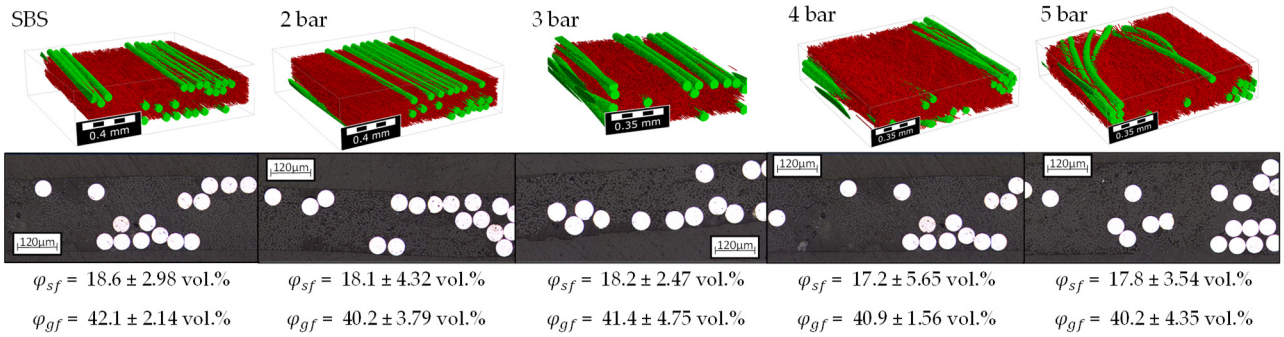

Figure 14. Three-dimensional scans and micrographs of the morphology of the hybrid tapes investigated in this study.

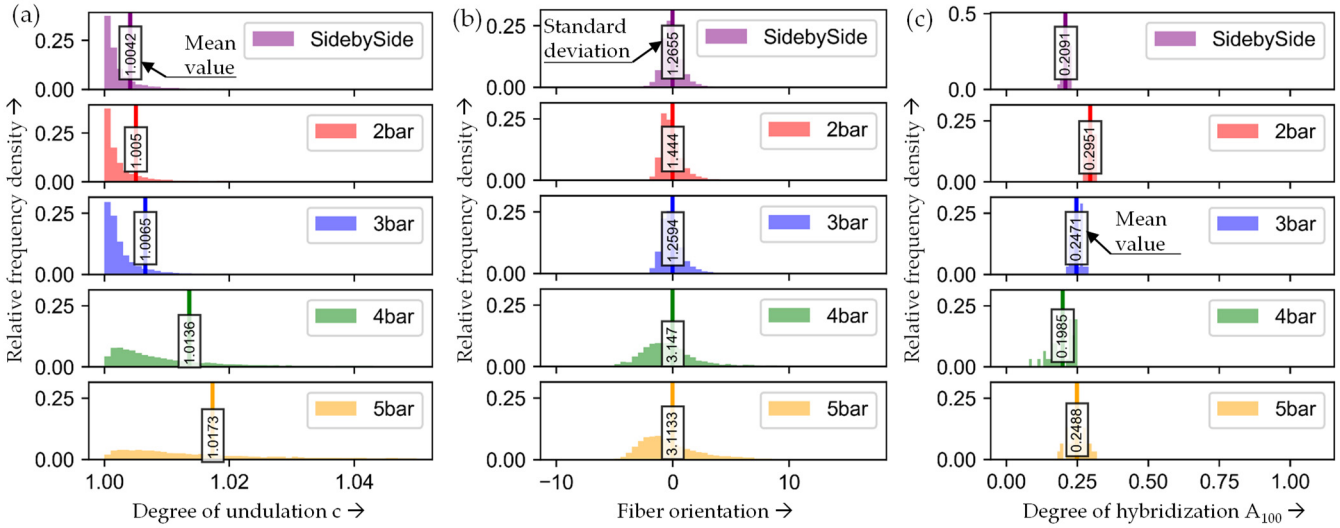

Figure 15. (**a**) The degree of undulation, (**b**) fiber orientation, and (**c**) degree of hybridization of the hybrid tapes investigated in this study.

Furthermore, it can be observed that both the degree of undulation (see Figure 15a) and the standard deviation of the fiber orientation (see Figure 15b) exhibit a slight reduction in comparison to the hybrid yarn configurations. It is postulated that this phenomenon is predominantly attributable to the pre-tension device of the winding frame in conjunction with the silicone rings at the deflection points of the winding shafts. Due to this setup, the multifilament yarns are subjected to slight tensile stresses when the pressing tool is closed, resulting in a stronger alignment of the fibers along the yarn orientation and a reduction in undulation. The outcomes of the mechanical characterization of the hybrid tapes are illustrated in Figure 16. With regard to stiffness (see Figure 16b), yield stress (see Figure 16c), and strength (see Figure 16d), the hybrid tapes display analogous characteristics to those observed in the hybrid yarns (see Figure 13b–d). The stiffness and yield stress of the tapes are modestly elevated in comparison to the respective characteristics of the hybrid yarns, while the strength values are significant lower ($\Delta\sigma > 100$ MPa). These observations can be attributed to a number of factors. Firstly, the lower degree of undulation and the reduced deviation in fiber orientation contribute to the increased stiffness. Secondly, the embedding of the fiber in the PP matrix results in a significantly more uniform load transfer into the fibers in comparison to multifilament yarns. This uniform load transfer leads to a more balanced stress state for the respective fibers. In contrast to the slightly cascading load transfer in undulated multifilament yarns, this also contributes to an increase in the stiffness of the hybrid tapes. The behavior of the yield point can be derived from that of the stiffness. The yield point is the result of the transition of the steel fibers from an elastic to an

elastic–plastic material behavior. Consequently, the elongation at the yield point of a hybrid tape only depends on the behavior of the steel fibers. Given equivalent strains in the fiber direction when the yield point is reached, the decline in stiffness implies a corresponding reduction in yield stress.

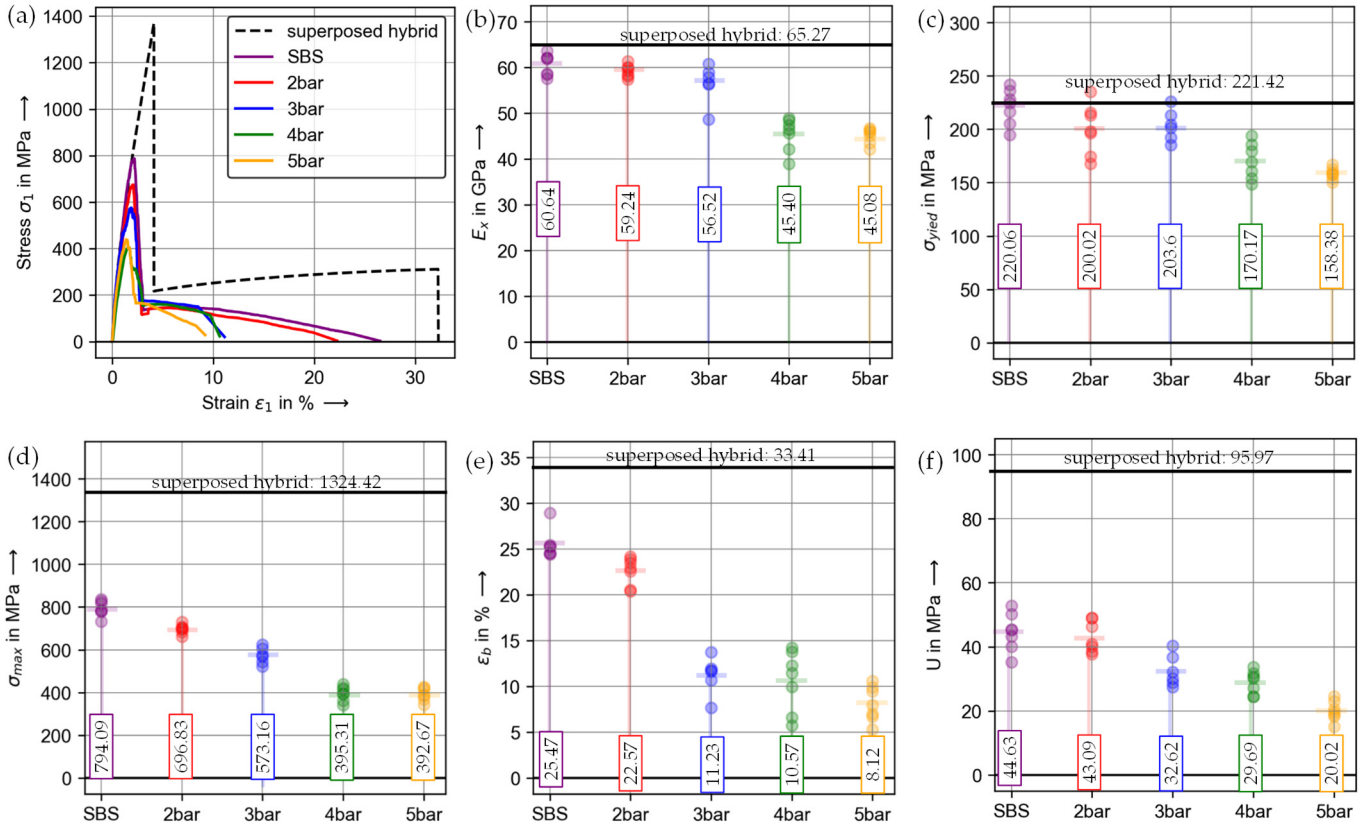

Figure 16. (**a**) Mean curves of the stress–strain behavior of the hybrid tapes and (**b**–**f**) an overview of the characteristic properties in the stress–strain behavior of the hybrid tapes. This includes the tensile stiffness Ex in (**b**), yield stress σ_{yi} in (**c**), initial failure stress σ_{ini} in (**d**), elongation at break ε_b in (**e**), and energy absorption U in (**f**).

The initial failure occurs when the glass fibers reach their strength limit. The lower strength values in comparison to the hybrid yarns can be attributed to pre-tensioning, which applies slight tensile stresses to the fibers when the pressing tool is closed. In combination with the fiber damage resulting from the hybridization process, this results in an additional reduction in tension values. Furthermore, it is observed that the elongation at break of the hybrid tapes (see Figure 16e), in contrast to the hybrid yarns, exhibits a notable decrease with the increase in air pressure during the hybridization process. While the discrepancies between the hybrid yarns and the hybrid tapes of the side-by-side and the 2-bar configuration are relatively moderate, with a $\Delta\varepsilon$ of approximately 5%. In contrast, the discrepancies between the hybrid yarns and the hybrid tapes are more pronounced at higher air pressures, reaching up to a $\Delta\varepsilon$ of approximately 22% for the 5-bar configuration. In this regard, it is postulated that this phenomenon is predominantly attributable to the increased undulation of steel fibers at increased air pressures. While the undulated steel fibers within a hybrid multifilament yarn align themselves along the yarn orientation when subjected to tensile loads, the steel fibers within a hybrid tape are prevented from realigning due to their embedding in the PP matrix. This prevents the plastic deformation potential of the steel fibers from being distributed across the entire sample, resulting in strain localizations and a reduced elongation at break. The energy absorption during the tensile test (see Figure 16f)

is a derived parameter that depends largely on the behavior of the strength and elongation at break. As the air pressure in the hybridization process increases, both the strength and the elongation at break of the hybrid tapes are reduced, which also effects the absorbed energy. In particular, the reduced elongation at break leads to significantly lower energy absorption, as the material shows less plastic deformation. In the comparison between the theoretical determined behavior of the superposed material and the measured properties of the hybrid tapes, the greatest discrepancies are observed in the strength, the elongation at break, and the absorbed energy. With regard to strength, these discrepancies can be attributed to the size effect and the fiber damage caused by the hybridization process, while the discrepancies regarding the elongation at break and the absorbed energy are primarily attributable to strain localization effects. The damage associated with the initial failure of the homogeneously dispersed glass and steel fiber-reinforced polypropylene (PP) differs significantly from the behavior observed in layer-separated hybridized metal fiber composites (see Figure 17a). In layer-separated hybrid laminates, damage induced by the initial failure typically occurs as delamination at the interfaces between the different types of fiber-reinforced layers. This delamination leads to a separation of the layers and spreads as a result of further stress until the laminate fails completely [33]. In contrast, the homogeneously hybridized glass and steel fiber-reinforced PP material exhibits different damage behavior. Here, damage occurs in the form of fractures along the fiber orientation. With increasing deformation, more and more fractures appear, ultimately leading to the complete failure of the hybrid laminate. The stress–strain behavior post failure can be divided into two distinct zones. In the initial zone, a slight increase in tensile stress is evident. This rise can be attributed to the load transfer by the remaining steel fibers, which remain intact despite the failure of the glass fibers (see Figure 17b).

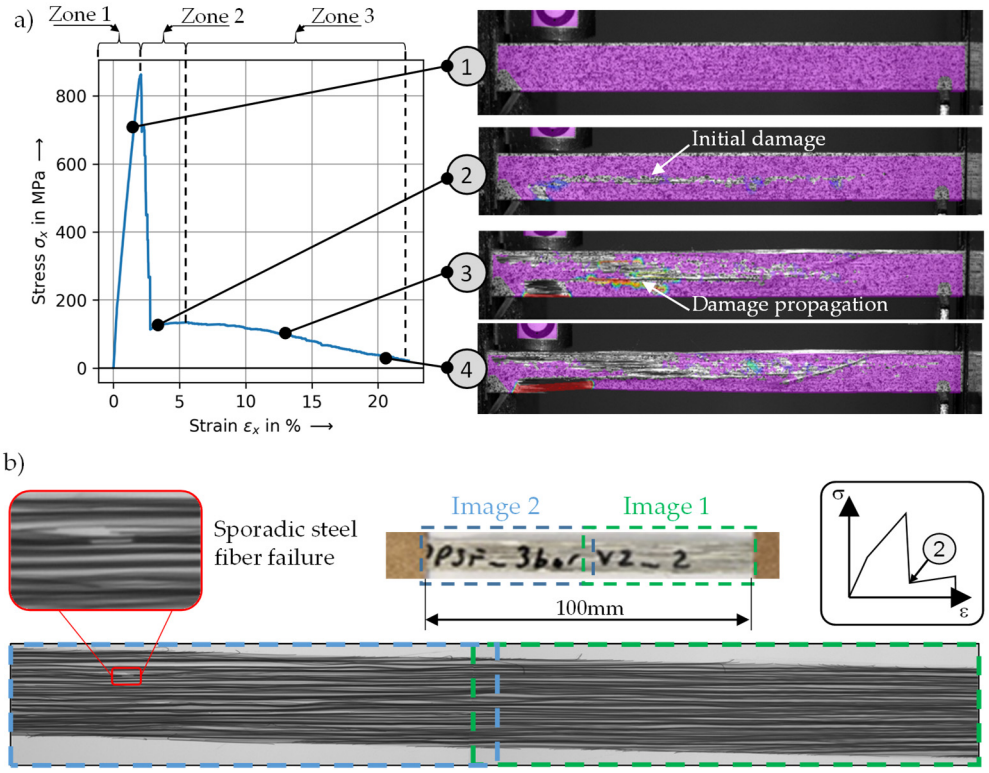

Figure 17. (**a**) Damage occurring in tensile tests of homogeneously hybridized glass and steel fiber-reinforced PP and (**b**) a radiographic image of a specimen in a state directly after the initial failure.

In the second zone, a gradual and uneven reduction in tensile stress is observed. This phase is characterized by the progressive cracking and failure of individual steel fibers,

which are no longer capable of bearing the remaining load. Given the uneven reduction in stress, it can be further postulated that the stress–strain behavior is influenced by the friction forces of steel fiber pull-out mechanisms. The observed behavior clearly demonstrates that the microstructure of the hybrid laminates significantly influences their damage behavior. The homogeneous mixing of the steel and glass fibers effectively prevents delamination and results in progressive damage along the fiber orientation.

4. Conclusions

This study explores the development and characterization of hybrid materials combining glass fibers, steel fibers, and polypropylene (PP) filaments, with a focus on understanding the effects of hybridization on mechanical properties, microstructure, and damage behavior. Hybrid yarns were manufactured using air jet texturing and subsequently processed into hybrid tapes via thermoforming. This study covered the entire manufacturing chain, from analyzing individual filament properties to hybrid yarn manufacturing and tape manufacturing. Microscopic and three-dimensional analyses revealed that higher air pressures (4–5 bar) during air jet texturing increase the degree of hybridization of steel and glass fibers but also lead to greater fiber undulation and deviations in fiber orientation. These topological influences negatively impact the mechanical properties, including reductions in tensile stiffness, yield strength, and yarn strength, primarily due to damage to the glass fiber during the hybridization process. Furthermore, the flow movement of the PP matrix during thermal pressing also effects the fiber dispersion and partly compensates for the effect from the air jet texturing process. Therefore, it is concluded that air jet texturing technology is unsuitable for hybridizing the selected steel and glass filaments. The underlying cause can be attributed to the inherent technological constraints associated with air texturing technology. The discrepancy in filament size, in conjunction with the specific material properties of the selected hybridization partners, results in a surpassing of these constraints. Nevertheless, the mechanical testing further highlighted a novel damage mechanism in homogeneously hybridized laminates. Unlike layer-separated laminates, where damage propagates between layers, laminates with micro-level hybridization exhibited fractures extending along fiber orientations, coupled with progressive fracturing of steel fibers and pull-out mechanisms. These phenomena create a gradual stress reduction in the post-failure behavior, confirming the initially postulated hypothesis that homogeneous hybridization enables alternative failure and energy absorption mechanisms. The findings from this study indicate the potential for the development and optimization of homogeneous dispersed metal fiber hybrid composites. Future research should focus on the development of a suitable hybridization process to achieve a targeted dispersion of different fiber types while simultaneously ensuring short flow paths and a significant reduction in fiber damage.

Author Contributions: J.R.: conceptualization, investigation, formal analysis, validation, and writing—original draft preparation. M.O.: writing—review and editing. S.S.: writing—review and editing, supervision, project administration, and funding acquisition. A.A.: writing—review and editing and project administration. C.C.: project administration and funding acquisition. All authors have read and agreed to the published version of the manuscript.

Funding: The German Research Foundation provided financial support for this study (DFG, SCHM 2726/6-1, CH 174/54-1).

Data Availability Statement: The datasets used during the current study are available from the corresponding author on reasonable request.

Conflicts of Interest: The authors declare no conflicts of interest.

References

1. Perkins, W.G. Polymer toughness and impact resistance. *Polym. Eng. Sci* **1999**, *39*, 2445–2460. [CrossRef]
2. Thanomsilp, C.; Hogg, P. Penetration impact resistance of hybrid composites based on commingled yarn fabrics. *Compos. Sci. Technol.* **2003**, *63*, 467–482. [CrossRef]
3. Baucom, J.N.; Zikry, M.A. Low-velocity impact damage progression in woven E-glass composite systems. *Compos. Part A Appl. Sci. Manuf.* **2005**, *36*, 658–664. [CrossRef]
4. Khalid, M.Y.; Arif, Z.U.; Ahmed, W.; Arshad, H. Evaluation of tensile properties of fiber metal laminates under different strain rates. *Proc. Inst. Mech. Eng. Part E J. Process Mech. Eng.* **2021**, *236*, 556–564. [CrossRef]
5. Hynes, N.R.J.; Vignesh, N.J.; Jappes, J.W.; Velu, P.S.; Barile, C.; Ali, M.A.; Farooq, M.U.; Pruncu, C.I. Effect of stacking sequence of fibre metal laminates with carbon fibre reinforced composites on mechanical attributes: Numerical simulations and experimental validation. *Compos. Sci. Technol.* **2022**, *221*, 109303. [CrossRef]
6. Costa, R.D.F.S.; Sales-Contini, R.C.M.; Silva, F.J.G.; Sebbe, N.; Jesus, A.M.P. A Critical Review on Fiber Metal Laminates (FML): From Manufacturing to Sustainable Processing. *Metals* **2023**, *13*, 638. [CrossRef]
7. Alderliesten, R.C. *Fatigue Crack Propagation and Delamination Growth in Glare*; Delft University Press: Delft, The Netherlands, 2005; ISBN 978-9040725883.
8. Wisnom, M.R. The role of delamination in failure of fibre-reinforced composites. *Philos. Trans. A Math. Phys. Eng. Sci.* **2012**, *370*, 1850–1870. [CrossRef]
9. Mamalis, D.; Obande, W.; Koutsos, V.; Blackford, J.R.; Ó Brádaigh, C.M.; Ray, D. Novel thermoplastic fibre-metal laminates manufactured by vacuum resin infusion: The effect of surface treatments on interfacial bonding. *Mater. Des.* **2019**, *162*, 331–344. [CrossRef]
10. Kuhtz, M.; Hornig, A.; Richter, J.; Gude, M. Increasing the structural energy dissipation of laminated fibre composite materials by delamination control. *Mater. Des.* **2018**, *156*, 93–102. [CrossRef]
11. Zimmermann, S.; Specht, U.; Spieß, L.; Romanus, H.; Krischok, S.; Himmerlich, M.; Ihde, J. Improved adhesion at titanium surfaces via laser-induced surface oxidation and roughening. *Mater. Sci. Eng. A* **2012**, *558*, 755–760. [CrossRef]
12. Salve, A.; Kulkarni, R.; Mache, A. A Review: Fiber Metal Laminates (FML's)—Manufacturing, Test methods and Numerical modeling. *Int. J. Eng. Technol. Sci.* **2018**, *3*, 71–84. [CrossRef]
13. Swolfs, Y.; Verpoest, I.; Gorbatikh, L. Recent advances in fibre-hybrid composites: Materials selection, opportunities and applications. *Int. Mater. Rev.* **2019**, *64*, 181–215. [CrossRef]
14. Swolfs, Y.; Gorbatikh, L.; Verpoest, I. Fibre hybridisation in polymer composites: A review. *Compos. Part A Appl. Sci. Manuf.* **2014**, *67*, 181–200. [CrossRef]
15. Czél, G.; Wisnom, M.R. Demonstration of pseudo-ductility in high performance glass/epoxy composites by hybridisation with thin-ply carbon prepreg. *Compos. Part A Appl. Sci. Manuf.* **2013**, *52*, 23–30. [CrossRef]
16. Czél, G.; Jalalvand, M.; Wisnom, M.R.; Czigány, T. Design and characterisation of high performance, pseudo-ductile all-carbon/epoxy unidirectional hybrid composites. *Compos. Part B Eng.* **2017**, *111*, 348–356. [CrossRef]
17. Swolfs, Y.; McMeeking, R.M.; Verpoest, I.; Gorbatikh, L. The effect of fibre dispersion on initial failure strain and cluster development in unidirectional carbon/glass hybrid composites. *Compos. Part A Appl. Sci. Manuf.* **2015**, *69*, 279–287. [CrossRef]
18. Rehra, J.; Andriß, C.; Schmeer, S.; Breuer, U.P. Describing the Material Behavior of Steel and Carbon Fiber Reinforced Composites Using a Combined Damage-Plasticity Approach. *J. Compos. Sci.* **2022**, *6*, 235. [CrossRef]
19. Rehra, J. *Beitrag zur Beschreibung des mechanischen Materialverhaltens von Metall-Faser-Hybrid-Verbund-Werkstoffen am Beispiel von stahl- und kohlenstofffaserverstärktem Epoxidharz*; Rheinland-Pfälzische Technische Universität Kaiserslautern-Landau: Kaiserslautern, Germany, 2023.
20. Schmeer, S.; Steeg, M.; Maier, M.; Mitschang, P. Metal Fibre Reinforced Composite—Potentialities and Tasks. *Adv. Compos. Lett.* **2009**, *18*, 096369350901800202. [CrossRef]
21. Di Benedetto, R.M.; Janotti, A.; Gomes, G.F.; Ancelotti Junior, A.C.; Botelho, E.C. Development of hybrid steel-commingled composites CF/PEEK/BwM by filament winding and thermoforming. *Compos. Sci. Technol.* **2022**, *218*, 109174. [CrossRef]
22. Adam, T.J.; Wierach, P.; Mertiny, P. Multifunctional Hybrid Fiber Composites for Energy Transfer in Future Electric Vehicles. *Materials* **2022**, *15*, 6257. [CrossRef]
23. Truong, G.T.; van Tran, H.; Choi, K.-K. Tensile behavior of on- and off-axis carbon fiber reinforced polymer composites incorporating steel wire mesh. *Mech. Mater.* **2019**, *137*, 103131. [CrossRef]
24. Swolfs, Y.; Cuyper, P.d.; Callens, M.G.; Verpoest, I.; Gorbatikh, L. Hybridisation of two ductile materials—Steel fibre and self-reinforced polypropylene composites. *Compos. Part A Appl. Sci. Manuf.* **2017**, *100*, 48–54. [CrossRef]
25. O'Brien, C.; McBride, A.; E Zaghi, A.; Burke, K.A.; Hill, A. Mechanical Behavior of Stainless Steel Fiber-Reinforced Composites Exposed to Accelerated Corrosion. *Materials* **2017**, *10*, 772. [CrossRef] [PubMed]
26. Callens, M.G.; Gorbatikh, L.; Verpoest, I. Ductile steel fibre composites with brittle and ductile matrices. *Compos. Part A Appl. Sci. Manuf.* **2014**, *61*, 235–244. [CrossRef]

27. Allaer, K.; Baere, I.d.; Lava, P.; van Paepegem, W.; Degrieck, J. On the in-plane mechanical properties of stainless steel fibre reinforced ductile composites. *Compos. Sci. Technol.* **2014**, *100*, 34–43. [CrossRef]
28. Acar, M.; Bilgin, S.; Versteeg, H.K.; Dani, N.; Oxenham, W. The Mechanism of the Air-Jet Texturing: The Role of Wetting, Spin Finish and Friction in Forming and Fixing Loops. *Text. Res. J.* **2006**, *76*, 116–125. [CrossRef]
29. Wickramasinghe, G.; Foster, P.W. Effects of core-yarn overfeed on texturing performance: Comparison between air-jet and steam-jet texturing. *J. Text. Inst.* **2016**, *107*, 291–299. [CrossRef]
30. Abdkader, A.; Khurshid, M.F.; Cherif, F.; Hasan, M.M.B.; Cherif, C. Development of an Innovative Glass/Stainless Steel/Polyamide Commingled Yarn for Fiber-Metal Hybrid Composites. *Materials* **2023**, *16*, 1668. [CrossRef]
31. Hasan, M.M.; Staiger, E.; Ashir, M.; Cherif, C. Development of carbon fibre/polyamide 6,6 commingled hybrid yarn for textile-reinforced thermoplastic composites. *J. Thermoplast. Compos. Mater.* **2015**, *28*, 1708–1724. [CrossRef]
32. Das, A.; Krishnasamy, J.; Alagirusamy, R.; Basu, A. Analysis of the electromagnetic shielding behavior of stainless steel filament and PET/SS hybrid yarn incorporated conductive woven fabrics. *Fibers Polym.* **2014**, *15*, 2423–2427. [CrossRef]
33. Overberg, M.; Hasan, M.M.B.; Rehra, J.; Lohninger, E.; Abdkader, A.; Cherif, C. Development of multi-material hybrid yarns consisting of steel, glass and polypropylene filaments for fiber hybrid composites. *Text. Res. J.* **2023**, *93*, 4865–4878. [CrossRef]
34. *ISO 5079:2020*; Textile Fibres—Determination of Breaking Force and Elongation at Break of Individual Fibres. German version DIN EN ISO 5079:2020; International Organization for Standardization: Geneva, Switzerland, 2021.
35. *ISO 527-4:2021*; Plastics—Determination of Tensile Properties—Part 4: Test Conditions for Isotropic and Orthotropic Fibre-Reinforced Plastic Composites. German version EN ISO 527-4:2021; International Organization for Standardization: Geneva, Switzerland, 2021.